



Originally published as:

Petricca, P., Carminati, E. (2016): Present-day stress field in subduction zones: Insights from 3D viscoelastic models and data. - *Tectonophysics*, 667, pp. 48–62.

DOI: <http://doi.org/10.1016/j.tecto.2015.11.010>

Present-day stress field in subduction zones: insights from 3D viscoelastic models and data

Patrizio Petricca^a, Eugenio Carminati^{b,c}

^a*GFZ German Research Centre for Geosciences, Potsdam, Germany*

^b*Dipartimento di Scienze della Terra, Sapienza Università di Roma, Rome, Italy*

^c*Istituto di Geologia Ambientale e Geoingegneria, CNR, Rome, Italy.*

Abstract

3D viscoelastic FE models were performed to investigate the impact of geometry and kinematics on the lithospheric stress in convergent margins. Generic geometries were designed in order to resemble natural subduction. Our models predictions mirror the results of previous 2D models concerning the effects of lithosphere-mantle relative flow on stress regimes, and allow a better understanding of the lateral variability of the stress field. In particular, in both upper and lower plates, stress axes orientations depend on the adopted geometry and axes rotations occur following the trench shape. Generally stress axes are oriented perpendicular or parallel to the trench, with the exception of the slab lateral tips where rotations occur. Overall compression results in the upper plate when convergence rate is faster than mantle flow rate, suggesting a major role for convergence. In the slab, along-strike tension occurs at intermediate and deeper depths (> 100 km) in case of mantle flow sustaining the sinking lithosphere and slab convex geometry facing mantle flow or in case of opposing mantle flow and slab concave geometry facing mantle flow. Along-strike compression is predicted in case of sustaining mantle flow and concave slabs or in case of opposing mantle flow and convex slabs. The slab stress field is thus controlled by the direction of impact of mantle flow onto the slab and by slab

*Corresponding author

Email addresses: petricca@gfz-potsdam.de (Patrizio Petricca), Phone: +49 331288-1959 (Patrizio Petricca)

longitudinal curvature. Slab pull produces not only tension in the bending region of subducted plate but also compression where upper and lower plates are coupled. A qualitative comparison between results and data in selected subductions indicates good match for South America, Mariana and Tonga-Kermadec subductions. Discrepancies, as for Sumatra-Java, emerge due to missing geometric (e.g., occurrence of fault systems and local changes in the orientation of plate boundaries) and rheological (e.g., plasticity associated with slab bending, anisotropy) complexities in the models.

Keywords: stress, subduction geometry, numerical viscoelastic modeling, absolute plates motion.

1. Introduction

The dynamics of subduction zones depend on the balance of driving and resisting forces (fig. 1a) and on the geometry, in turn controlled by plate-scale processes and paleogeography. In addition, mantle flow affects the sinking rate and the geometry of the subducting lithosphere (Rodríguez-González et al., 2014).

Tomographic studies indicate that subducted slabs are not simple 2D features (e.g., Zhao, 2004; Obayashi et al., 2013). Slab shape changes not only along-dip, but also along the length of many arcs. Therefore, slab geometry must be described by its dip, lateral extent and shape (i.e., straight or curved, with direction of concavity when curved). As far as the slab dip is concerned, significant effort has been spent in the literature to explain the observed variability. Dickinson (1978) and Uyeda (1981) first noted the evident differences between shallow and steep subduction zones, discriminating two end member styles of subduction: the Chilean-type (fig. 1b) and the Mariana-type (fig. 1c). In addition to the difference in the slab dip-angle (e.g., Ricard et al., 1991; Doglioni, 1993), the corresponding characteristics for the two classes are (Doglioni et al., 2007, and references therein): maximum depth of seismicity (300 km vs 700 km, respectively); state of stress in the back-arc region (compressive vs exten-

sional); state of stress in the slab at intermediate depths (down-dip tensional vs down-dip compressional); structural elevation and vergence of the accretionary wedge (low-elevated single-verging vs high-elevated double-verging); subsidence rate in the foredeep (low vs high); thin- vs thick-skinned tectonics.

Considering the third dimension, both arcuate and straight subduction zones exist. Frank (1968) first noted that the curvature of subduction zone trenches and arcs varies considerably on Earth (fig. 2), from concave toward the mantle wedge (e.g., Aleutians-Alaska, Scotia, Calabria, Hellenic, North Ryukyu, Marianas, Sumatra; Hsui & Youngquist (1985); Mahadevan et al. (2010)), to straight (e.g., Tonga-Kermadec, South Solomon, Central America, Vanuatu), to convex (e.g., North Solomon, South Ryukyu, Central-South America, Cascadia; Morra et al. (2006)).

Subduction zones and their associated slabs are limited in lateral extent (with lengths spanning in the 250-7400 km range). Their three-dimensional geometry evolves over time (Schellart et al., 2007) and can often be quite complex (Jadamec & Billen, 2010).

The dynamics of plate margins is also affected by plate convergence and by the absolute plate motion (e.g., Doglioni et al., 1999; Carminati & Petricca, 2010; Rodríguez-González et al., 2014). Hotspot tracks provide a reference frame for the absolute motion of plates (e.g., Norton, 2000), indicating that a relative motion occurs between the lithosphere and the underlying deep, high-viscosity mantle (Net Rotation; e.g., Ricard et al., 1991), the asthenosphere likely acting as a detachment layer owing to its low viscosity (e.g., Panza et al., 2010). The eastward mantle flow velocity depends on the adopted assumptions (e.g., Gripp & Gordon, 2002; Steinberger et al., 2004; Cuffaro & Jurdy, 2006; Crespi et al., 2007; Becker, 2008), ranging from 2 cm/yr to a maximum value of 13.4 cm/yr.

Using three-dimensional numerical simulations of free subduction, Schellart et al. (2007) showed that the 3D effect mainly operates close to the lateral edges of slabs. As a consequence, 2D simulations (e.g., Giunchi et al., 1996; Gardi et al., 2002; Carminati & Petricca, 2010) apply best to portions of wide slabs far from the slab edges, while for a full descriptions of the stress pattern a third

dimension is needed. Few 3D models of subduction considering viscoelastic rheologies are available in the literature (Negredo et al., 1997, 1999; Hashima et al., 2008), and no one concerns with the lateral variability of stress within the slab. This means that no systematic studies were dedicated to understand the factors controlling the variability of states of stress observed in natural subductions. With this study we aim at bridging this gap. For this purpose we built several numerical viscoelastic models characterized by 3D geometries inspired by the variability observed in natural subductions. The efficiency of the slab gravitational pull, the relative motion between upper and lower plates and mantle and lithosphere were investigated as controlling forces over the present-day stress field. The generic 3D geometries (although not simulating specific subduction zones) were specifically designed after a review of available databases of subduction zones geometries (e.g., Gudmundsson & Sambridge, 1998; Hayes et al., 2012; Basili et al., 2013, and references therein).

In the following, we first discuss the characteristics of the state of stress at crustal depths and within the slabs in subductions worldwide using the World stress map database (Heidbach et al., 2008). After evaluating the compatibility of 3D simulations results with respect to previous 2D models (Carminati & Petricca, 2010), we focus on along-strike deformation and stress axes rotations within the lower plate and on the stress field in the upper plate. Modeling results are then compared with stress data available for selected subductions whose geometries are similar to those modeled and consistencies and inconsistencies are discussed.

2. Stress field in natural subduction zones

In natural subductions the crustal stress field (depth 5-50 km) is extremely variable. In the lower plates, a transition from tension to compression with depth is described by shallow seismicity in the trench-outer rise (e.g., Seno & Yamanaka, 1996). Extension is consistent with the bending of the plate prior to subduction and compression at crustal depths is related to the coupling between

upper and lower plates, which generates the largest earthquakes worldwide (e.g.,
 Barrientos & Ward, 1990; Stein & Okal, 2005; Fujii et al., 2011). Few stress
 data are available for the non-subducted portion of lower plates. Available data
 show that the stress field is here generally characterized by tensional regimes
 and maximum horizontal stress (red axes in fig. 3, hereafter SHmax; Heidbach
 et al., 2008) sub-parallel to the trenches. This pattern means extension (σ_3)
 perpendicular to the trench and is related to the stretching due to the bending
 of the plate. Strike-slip and compressional regimes (green and blue axes in fig.
 3) do not follow any particular trend, and are generally observed around the
 trench lateral edges or in regions of strong interactions between mantle flow
 and complexly shaped slabs (i.e., trench deflections, slab lateral terminations
 or lithospheric discontinuities). Best examples come from the eastern edge of
 the Central America (fig. 3c), the northern edge of the Kermadec-Tonga (fig.
 3g), the eastern edge of the Aleutians-Alaska (fig. 3f) and the lateral edges of
 the Ryukyu subductions (fig. 3h). The stress field in the upper plates shows
 the highest variability. What one might expect in a convergent setting is over-
 all trench-perpendicular compression. This is true in several cases (e.g., South
 America, Sumatra, Central America, Vanuatu and Solomon; see fig. 3a-e), but
 extensional processes characterize upper plates of other subductions. These
 tensional stresses are described by SHmax parallel to the slab trench and are
 associated with the development and evolution of back-arc basins. The best
 example is the upper plate of the Izu-Bonin subduction (fig. 3i), where a ten-
 sional stress pattern can be tracked from north to south, parallel to the strike
 of the trench (i.e., extension perpendicular and SHmax parallel to the trench).
 The same stress field characterizes the Kermadec (fig. 3g) and the Aleutians
 subductions (fig. 3f), although less clear from data. In subductions governed by
 overall trench-perpendicular extension, local compression can affect the upper
 plate in regions lying over the slab projection on the surface. Local trench-
 perpendicular compression occurs in the upper plate of the Aleutians (fig. 3f),
 the Kermadec (fig. 3g) and the Ryukyu (fig. 3h) subductions, generally char-
 acterized by trench-perpendicular extensional processes.

111 Focusing on the orientation of stress axes, a large variability mirrors the
 112 differences in the geometry of trenches. In east dipping subductions (generally
 113 sustained by the eastward relative mantle flow; fig. 1b) the lithosphere in the
 114 upper plate shows a compressional regime and typical trench-perpendicular or
 115 sub-perpendicular direction for SHmax axes (blue axes in fig. 3a-e). In west
 116 dipping subductions (generally opposed by the mantle flow; fig. 1c) the stress
 117 field is tensional (with tension perpendicular to the trench) in the upper plate as
 118 indicated by SHmax axes sub-parallel to the trench (red axes in fig. 3f-j). This
 119 pattern is maintained along the strike of linear trenches (e.g., Chile, Solomon and
 120 Kermadec) or it adapts in case of trench deflections (e.g., Sumatra, Aleutians
 121 and Mariana). Major rotations affect the stress axes approaching the trench
 122 lateral edges (e.g., north of Vanuatu or east of Alaska; see fig. 3d and f). As a
 123 specific example, the lithosphere in the upper plate of the South America margin
 124 is under compression and shows preferentially SHmax axes sub-perpendicular
 125 to the trench (fig. 3a). The stress field is laterally maintained along the straight
 126 portions of the subduction (e.g., in the Chile region). A clear reorientation
 127 of the stress axes coincides with the trench deflection moving northward (i.e.,
 128 in the South Peru area). Again thrust faulting regimes emerge in the Central
 129 America subduction (fig. 3c), and the straight portions of the Solomon subduc-
 130 tion trench (fig. 3e), with SHmax axes perpendicular to the straight trenches.
 131 The progressive rotation of SHmax axes from a NE-SW direction (in its western
 132 part) to an approximately N-S direction (to the east), still perpendicular to the
 133 plate boundary, is associated with the smooth curvature of the Sumatra-Java
 134 subduction (fig. 3b).

135 A complete description of deformation in subduction systems requires also a
 136 description of the stress state affecting the subducting slab. From focal mecha-
 137 nisms of earthquakes, the stress field reconstructed for intermediate depths (fo-
 138 cal depths between 100 km and 300 km; Isacks & Molnar, 1971) can range from
 139 down-dip tension to down-dip compression (Bailey et al., 2012). At intermedi-
 140 ate depths, bending and unbending (fig. 1a) have been invoked as the cause of
 141 double seismic zones with opposing stresses in the upper and lower interfaces of

the slab (Engdahl & Scholz, 1977; Kawakatsu, 1986), usually showing down-dip compression and tension respectively (Hasegawa et al., 1978). Deep earthquakes (300-700 km) are typically down-dip compressional in all Wadati-Benioff zones that reach the upper-lower mantle boundary, reflecting the increasing resistance encountered by the subducting lithosphere (Isacks & Molnar, 1969, 1971) at the viscosity jump affecting the 670 km discontinuity and the slab positive buoyancy anomalies induced by thermally down-warped perovskite-forming reactions at these depths (fig. 1a). As a first approximation, density driven slab pull generates down-dip extension in the slab (e.g., Anderson, 2001; Conrad & Lithgow-Bertelloni, 2002), while viscous resistance to penetration into the lower mantle results in down-dip compression, that propagates up-dip along slabs toward intermediate depths depending on the magnitude of this deep-seated positive buoyancy (Chen et al., 2004).

3. Model description

The 3D modeling was performed using the finite elements method, with a viscoelastic approach. Our models simulate the subduction of an oceanic plate under a continental plate (fig. 4). The compatibility ($\varepsilon = \nabla \vec{s}$, where ε = strain and \vec{s} = displacement), equilibrium and constitutive equations for a viscoelastic Maxwell body were solved simultaneously using the software COMSOL Multiphysics (<http://www.comsol.com/>).

Viscoelastic materials have been widely used in the literature to simulate stress distribution in slabs (Giunchi et al., 1996; Carminati et al., 1999; Negredo et al., 1999; Gardi et al., 2002; Carminati & Petricca, 2010; Petricca et al., 2013). The constitutive equation is:

$$\delta \varepsilon_{Total} / \delta t = (\sigma / \eta) + 1/E (\delta \sigma / \delta t) \quad (1)$$

The equilibrium equations account for the balance of internal and external forces. With F defining the volume forces, the formulation becomes:

$$\nabla\sigma + \mathbf{F} = 0 \quad (2)$$

The assumptions, rheological parameters, geometries and forcing factors adopted in our simulations will be now discussed.

3.1. Rheology

The elastic rheological parameters used in this work are based on the PREM model (Dziewonski & Anderson, 1981), while the adopted mantle viscosity values are consistent with literature studies for the upper mantle (Spada et al., 1992; Kaufmann & Lambeck, 2000; Nakada & Lambeck, 1989) and for the lithospheric mantle (Houseman & Gubbins, 1997). The adopted rheological parameters are also in line with previous viscoelastic models of subductions (e.g., Negredo et al., 1999; Giunchi et al., 1996; Gardi et al., 2002, 2010).

The models represent the Earth through three-dimensional portions of a convergent margin that extend from the topographic surface down to a maximum depth of 1000 km. All the models include the crust, the lithospheric mantle, the asthenosphere, the upper mantle and part of the lower mantle. For every region of the model, materials are defined by their elastic properties (Young modulus E and Poisson coefficient ν) and the dynamic viscosity (η) (table 1).

Our models do not include rheological and density changes associated with the olivine-wadsleyite phase transition. For a discussion on the contrasting effects of this phase transition on the density anomaly of sinking slabs, the reader should refer to Bina (1996, 1997), Tetzlaff & Schmeling (2009), Lee & King (2011), Quinteros & Sobolev (2013) and to the following discussion. As in previous studies (e.g., Giunchi et al., 1996), our models assume that the former stress in the system has been released by creep and seismic activity at the moment of starting calculations.

3.2. Model geometries

In agreement with average global values, the continental lithosphere has a thickness of 85 km, including a 35 km thick crust and 50 km thick lithospheric

mantle. The oceanic lithosphere is 60 km thick due to 10 km thick crust summed with 50 km of lithospheric mantle. In order to test the effects of varying the coupling between lithosphere and mantle by gradually lowering its viscosity in different models, an asthenosphere approximately 200 km thick (i.e., down to a depth of 300 km) was introduced. The asthenosphere (or low velocity zone) was modeled in some runs as a distinct layer because of its lower viscosity with respect to the rest of the upper mantle (Anderson, 1989). The assumed thickness is consistent with natural observations ranging from 100 to 400 km (e.g., Gung et al., 2003). However our results show (accompanying material) that the lithosphere/mantle coupling does not affect the stress regime and direction (we are interested for), but only the stress magnitude. As a consequence, results shown in the main text come from models considering the mantle as a homogeneous layer. The effects of imposing an asthenosphere viscosity lower than that of the remaining mantle will be briefly discussed. A fundamental arrangement in the design phase was to split the subducting slab into sub-domains, needed during the process of model setup to force negative buoyancy anomalies (fig. 4a).

In agreement with previous studies (e.g., Giunchi et al., 1996; Petricca et al., 2013; Zhong et al., 1998), the contact between upper and lower plates is modeled as a single fault, considered locked in all the calculation. This choice is motivated by the fact that we are interested in the regional stress field (compression or tension axes direction), rather than in stress magnitude (controlled by the upper-lower plate coupling). However, the maximum deviatoric stress that we obtain in our solutions along the interface domain never exceeds 250 MPa (auxiliary material fig. AUX1), similarly to previous studies (e.g., Giunchi et al., 1996).

Our models are truly three-dimensional, since the slabs are laterally finite. The mesh is designed using tetrahedral elements with nodal distance ranging between 12 km (lithosphere, slab and mantle surrounding the slab) and 300 km (at the bottom of the model). Planes of symmetry were used to halve the geometries in order to simplify the calculations, making the models less time and memory consuming. The effects of slab dip variations on the stress field

were addressed in previous works (Carminati and Petricca, 2010). Thus, in this paper we analyze the effects of the lateral finiteness of slabs rather than of slab dip. The following geometries were tested:

- 3D models with linear trench (fig. 4b): different lateral extent for the trench (in the range between 500 to 3000 km) provides a good representation of almost all known cases of linear worldwide subduction (e.g., from the laterally short Makran subduction to the 3000 km long Chile subduction; fig. 2).
- 3D models with curved trench: these models are meant to simulate convergent margins described by a curved slab shape, a feature common to subduction arcs. In a first set of geometries concave downward slabs are simulated (hereafter concave; fig. 4c). This geometry of slabs is typical of retreating hinge subduction. Slabs with a concave upward shape were also modeled (hereafter convex; fig. 4d), corresponding to several advancing hinge subduction zones. Several lateral lengths of slabs (from 500 km to 3000 km along strike) were tested in order to represent the variety of natural cases, starting from the smallest Calabrian and Nova Scotia arcs, up to the largest Aleutian and Sumatran arcs.

Only the intermediate case (i.e., 1000 km lateral extent of halved slab) of the described geometries are shown in fig. 4.

3.3. Model boundary conditions

Different kinematic scenarios are recognizable in natural subductions. The mantle flow and the slab dip can be toward the same direction or they can oppose either with curved or linear trenches (fig. 3). A list of the main subductions and their principal features is provided in table 3.

Mantle flow impacts the slabs at different rates, either supporting (e.g., in the South America, Sumatra, Central America, Vanuatu and Solomon) or opposing (e.g., in the Aleutians, Kermadec, Ryukyu, Izu-Bonin and Philippines) the subduction (see table 3). The effects of subduction kinematics variability

are tested in our models. The forces acting alternately or simultaneously are defined as boundary conditions and as body forces (fig. 4). The forcing processes that were simulated are: slab pull, mantle flow and plate convergence. As widely adopted in the literature (e.g., Giunchi et al., 1996; Negredo et al., 1999), gravity is not applied as a body force through the models, but is considered an adjunctive sub-domain condition acting on the upper surface of the model (Winkler foundation; Williams & Richardson, 1991) as a vertical pressure equal to $-\Delta\rho gv$ (where $\Delta\rho$ is the difference between crust and air densities, g is the gravity acceleration and v the vertical displacement). This representation of isostatic forces allows us to consider the density variations only in volumes affected by gravity anomalies. Slab pull, is simulated imposing the density anomaly in the deepest part of the slab (i.e., from 200 km down to the lower tip of the slab). Given the difficulty in evaluating the precise magnitude of slab pull in real subductions, a constant value of 60 kg/m³ in the density anomaly was used, consistent with seismological data (Yoshii, 1973). The chosen value represents a good average of those proposed in the literature, ranging between 50 kg/m³ (obtained with thermo-viscous models of slow subductions; e.g. Davies & Stevenson, 1992) and 100 kg/m³ if the eclogitization of lower crustal gabbros is taken into account. Otherwise, it has to be emphasized that seismological data suggest no slab pull in natural slabs (e.g., Ionian oceanic subduction Brandmayr et al., 2011). Owing to the uncertainty in the depth range and efficiency of slab pull, some runs were made adopting shallower density anomalies (from lithosphere bottom downwards) or no slab pull.

Plates convergence and mantle flow are simulated via a prescribed displacement condition over the boundary surfaces of the involved sub-domains (fig. 4). The velocity is imposed at the model lateral boundary as a horizontal displacement calculated at each time step multiplying the velocity by the duration of the time step. The bottom of the models, located within the lower mantle, is free to move in the tangential direction while zero displacement is allowed in the direction perpendicular to the boundary. A free boundary is imposed at the sides of the lower mantle while the lithospheric lateral boundaries are kept

fixed in the horizontal direction if no plate convergence is simulated. A free boundary condition is applied to the upper mantle lateral boundaries, if no asthenospheric flow relative to the lithosphere is imposed. Free slip is imposed at the other planes that bound the modeled domains. A list of modeled geometries can be found in table 2.

The whole set of models (described in the accompanying material) was run assuming convergence rates varying between 0 and 4 cm/yr and mantle flow rates varying between 0 and 8 cm/yr, to simulate the variability of mantle flow velocity predicted by plate kinematic models available in the literature.

Contrary to thermo-mechanical approaches (see Gerya, 2011, and references therein) and in agreement with previous works (e.g., Gardi et al., 2010), our models do not aim to simulate the initiation and the progressive evolution of subduction, but rather to study the actual stress regime by exploring the control exerted by different geodynamic processes. This approach implies computations simulating the evolution of subduction zones during relatively short time spans. All the models were initially solved through a static analysis. This approach is required to ensure an initial balance between the applied forces and the internal initial deformation of the system. Then, the static solution was used as an initial condition for the transient analysis. For the adopted viscoelastic materials, the steady state of the solutions is always achieved in a time of model evolution of 250 kyr. Such time span is smaller than the relaxation time assumed for crustal rocks, so that in our models the crust behaves largely in an elastic way. The models results are shown for the 250 kyr time, which is sufficient in this kind of models to reach a dynamic equilibrium between tectonic and isostatic forces, and for stress and strain rates to reach steady-state values (fig. AUX1). Similar time spans (200-250 kyr) to reach steady state were obtained in previous studies (Gardi et al., 2010; Giunchi et al., 1994, 1996). In the accompanying material the solutions for longer evolution times are shown (fig. AUX2).

314 4. Results

315 4.1. State of stress in slabs

316 The states of stress obtained within subducting slabs for the intermediate-
 317 length 3D geometries (see fig. 4 and table 2) are shown in fig. 5. Since the shape
 318 of the slab is closely linked to the dynamics of the subduction system, the results
 319 obtained for convex subduction geometry are shown for models characterized
 320 by mantle flow sustaining the slab (fig. 5a) and results for concave geometry are
 321 shown for models including mantle flow opposing the subduction (fig. 5c). The
 322 model with linear subduction geometry is forced only by slab pull (fig. 5b), and
 323 is thought to represent the initial phase of retreating slabs. The results of 3D
 324 models are consistent with the findings of the 2D models proposed by Giunchi
 325 et al. (1996) and Carminati & Petricca (2010): mantle flow opposing slabs
 326 enhances down-dip compression, whereas mantle flow sustaining slabs enhances
 327 tension.

328 A major difference with respect to 2D models is that, if mantle flow is
 329 applied, substantial along-strike deformation occurs within the subducted plate.
 330 If mantle flow opposes a concave slab (fig. 5c), two sets of tensional axes can
 331 be distinguished: 1) those associated with the down-bending of the lithosphere
 332 (as seen in 2D models and for the linear trench models), which characterize
 333 the shallow bending region and tend to rotate towards the slab lateral edges;
 334 2) those related to the slab differential retreat induced by the mantle push.
 335 The latter are mainly along-strike oriented and affect intermediate and deeper
 336 regions of the slab. Down-dip and along strike axes form a compression-tension
 337 couple that rotates moving towards the slab lateral edges.

338 If sustaining mantle flow is imposed over a convex slab (fig. 5a) tension,
 339 associated with slab pull and plate bending, still takes place at shallow depths.
 340 In addition, overall down-dip tension is observed at intermediate and deeper
 341 depths and along-strike tension occurs in central and lateral slabs domains.
 342 The compression-tension couples discussed earlier, are in this case replaced by
 343 tension-tension couples (respectively down-dip and along-strike). Inverting the

adopted mantle flow direction for the curved geometries (fig. AUX3), reverse stress states are obtained. If mantle flow is forced to sustain a concave slab, the down-dip compressional and along-strike tensional axes of fig. 5c turn into down-dip tensional and along-strike compressional. The opposite occurs if mantle flow opposes a convex slab, forcing down-dip and along-strike compression within the sinking lithosphere (fig. AUX3). In both cases, along-strike compression is due to the lateral push of the slab against the confining mantle. In addition, when the mantle flow parallels the slab interface, along-strike compression or tension occur because the lithosphere is squeezed or stretched in that direction (fig. AUX3).

4.2. Models stability

To verify the stability of the models, simulations were also performed varying the rheological parameters of lithospheric mantle and asthenosphere. The viscosity of the lithospheric mantle was varied between 10^{21} Pa s and 10^{23} Pa s. A low viscosity lithospheric mantle (e.g., 10^{21} Pa s) sustains little stresses. Increasing viscosity allows the lithosphere to sustain larger stresses. These effects on stress magnitudes are also emphasized in the upper plate and in the bending part of the slabs (fig. AUX4). Imposing a 200 km thick asthenosphere (fig. AUX5), to generate a more efficient decoupling between the lithosphere and the upper mantle, does not affect significantly the described stress patterns. A viscosity contrast of 1.5 orders of magnitude between lithosphere and upper mantle (i.e., 5×10^{22} in the lithospheric mantle versus 10^{21} Pa s in the upper mantle, as in the reference models) is sufficient to provide enough decoupling between the subducting slab and the surrounding mantle.

The mantle flow rate controls also the magnitude of both down-dip and along-strike stress within slabs. Obviously, as already discussed for 2D models by Carminati & Petricca (2010), the higher the speed, the larger the stress magnitude. The results of the sensitivity analysis suggest that even changing significantly the viscous parameters, the main predictions of our models are maintained.

374 *4.3. State of stress in the crust*

375 The effects of using 3D geometries are even clearer in map view. Slicing the
376 models at 5 km depth and considering the upper plate, the stress field shows
377 overall trench-perpendicular compression when only slab pull is applied (fig. 6a-
378 c) or if a sustaining mantle flow is added (fig. 6d-f). If subduction is forced by
379 an opposing mantle flow (fig 6g-i), the overriding plate is characterized by over-
380 all tension. Despite the general tensional stress field, a region of the overriding
381 plate is always characterized by trench-perpendicular compression. This area
382 is located within the lithosphere lying above the slab projection, and follows
383 the linear or curved trend of the slab (fig. 6). The stability of this feature is
384 evaluated by comparison with models with no slab pull or with increased slab
385 pull (from the lithosphere bottom to the lower slab tip). Results show that
386 in case of sustaining mantle flow, the stress field in the upper plate is steadily
387 compressional (fig. AUX6 a-c). In case of opposing mantle flow, the discussed
388 tension-compression-tension pattern occurs in the upper plate, and the larger
389 the slab pull the longer are the compressional stress axes and the narrower is
390 the strip of tension near the subduction trench (fig. AUX6 d-f).

391 Concerning the lower plate, the stress field at shallow depths is generally
392 neutral to tensional when the model is forced only by slab pull, or in case of
393 sustaining mantle flow (fig. 6a-f). Instead, widespread compression is gener-
394 ated by mantle flow opposing the sinking slab (fig. 6g-i). If plate convergence
395 is forced, the shallow lithosphere (depth of 5 km) undergoes overall compres-
396 sion as described for 2D models (Carminati & Petricca, 2010). This is true for
397 lithospheric convergence rate comparable to or faster than mantle flow rate (fig.
398 AUX7).

399 Shallow compressional axes have a constant (trench-perpendicular) orien-
400 tation along straight plate boundaries, while they rotate following the trench
401 curvature to maintain a trench-perpendicular orientation in curved subductions
402 (fig. 6). Far from plate boundaries the influence of geometry ceases and stress
403 axes tend to parallel the mantle flow. Stress axes rotations occur in both upper
404 and lower plates close to the lateral termination of the subducted lithosphere.

Larger rotations are predicted in linear trench case sustained by mantle flow (fig. 6d) and, to a lesser extent, in convex subductions sustained by mantle flow (fig. 6f) or concave subductions opposed by mantle flow (fig. 6h). In these regions, the axes directions may reflect the direction of the mantle drag (e.g., Petricca et al., 2013), that rotates around the lateral slab tip.

At greater depths (i.e., in slices cut at 50 km), the stress magnitude in the lithosphere decreases (fig. AUX7), but the stress orientations remain identical. The slab's lateral length controls the stress field less efficiently than the trench shape. In models characterized by large trench lateral length, stress axes rotation does not affect the central part the subduction system. In other words, the larger the slab's lateral extent, the more peripheral is this rotational effect related to lateral slab termination (fig. AUX8).

4.4. Comparison with World Stress Map data

The geometries of our models are generic. Although they were designed in order to resemble natural subduction zones, they do not faithfully represent specific subductions. Keeping in mind this limitation, natural subductions were selected for comparison with model results first by geometric similarity and second on availability of stress data. We excluded Vanuatu and Solomon subductions that show articulate trenches, Japan that is considered a non-standard case of W-directed subductions (e.g., Doglioni et al., 2007), central America that is characterized by oblique convergence and the Philippines because of the very sparse stress data (see fig. 3). Marianas is preferred to the Aleutians because is the typical W-directed subduction. Data from the World Stress Map (WSM, Heidbach et al., 2008) and classifications of the state of stress of upper plates (Heuret & Lallemand, 2005) are used for a comparison with model results at crustal depths.

As the WSM data show SHmax axes (i.e., σ_1 in compressional and strike-slip domains, σ_2 in tensional areas), while our results show maximum compression (σ_1) or tension (σ_3) stress axes, tensional SHmax axes from WSM in figures 7 and 8 were rotated by 90 degrees to allow direct comparison with our results.

Conversely, compressional SHmax from WSM and maximum compression directions from our models can be directly compared. Moreover, when comparing stress data with our results, it should be kept in mind that the state of stress of plates is controlled by the stresses imposed at all the boundaries of plates (e.g., Meijer & Wortel, 1999). In our simulations we force the model simulating the kinematics of subduction zones forcing convergence to the right and left boundaries, whereas the other boundaries are left free. This means that the resulting stress field is the result of the sole subduction process and should be summed with the stress field rising from other boundary conditions to be fully comparable with specific cases, as shown by Petricca et al. (2013) for the central Mediterranean area. Discrepancies between our models results and stress data will be discussed.

4.4.1. Upper plate - sustaining mantle flow kinematics

In fig. 7, results of models forced by a sustaining mantle flow (advancing hinge subductions) are compared with stress fields from natural subductions. All models in which subductions are sustained by mantle flow, predict compression in the upper plate and tension in the lower plate (fig. 7c-d). Smaller tension is predicted in the lower plate for concave geometries (fig. 7c). Compression predicted by models of subductions sustained by mantle flow is generally confirmed by seismic data, although a large variability occurs. Heuret & Lallemand (2005) classified strain of subduction zones upper plates using focal mechanisms of earthquakes occurring at a crustal depths. In their classification, among subductions sustained by mantle flow, Alaska and South America (Colombia, Peru, Chile, Juan Fernandez) subductions are characterized by upper-plate compression. Sumatra, Java and Cascadia have neutral stress states. Andaman is characterized by tension and Central America is characterized by prevailing strike-slip tectonics.

The concave shaped Sumatra-Java subduction (fig. 7a), and the convex part of the South America subduction corresponding with the trench at 20 south latitude (fig. 7b) were selected for more detailed comparisons and to highlight

consistencies and discuss the sources of inconsistencies between results and data. Away from slab edges, trench-perpendicular compression characterizes the South America margin, in agreement with modelling results. In the upper plate, strike-slip axes are abundant in the Sumatra subduction. Tension is also very diffuse and does not follow any particular trend. These observation is at odds with modeling results, with the exception of the easternmost part where compression perpendicular to the trench clearly emerges (fig. 7a).

4.4.2. Upper plate - opposing mantle flow kinematics

Upper plate tension predicted by our models of subductions opposed by mantle flow is consistent with seismic data (Heuret & Lallemand, 2005) that show less variability with respect to subductions sustained by mantle flow. Among subductions opposed by mantle flow, Ryukyu, Mariana, Izu-Bonin, Kamchatka, Antilles, Sandwich, Tonga-Kermadec are characterized by upper-plate tension, whereas Japan and Kuril are characterized by compression. The linear Kermadec-Tonga (fig. 8a) and the curved Mariana (fig. 8b) subductions were selected for more detailed comparison with models forced by opposing mantle flow (retreating hinge subductions). σ_3 axes of the World stress map run mostly perpendicular to the plates boundary in the upper plate of the Kermadec-Tonga and Mariana subductions (fig. 8a-b). Trench-perpendicular tension is generally reproduced in the upper plate of models forced by mantle flow opposing the subducting slab (fig. 8c-d). Both in curved and linear models, stripes of trench-perpendicular tension are predicted close to the trench and far from the trench, separated by trench perpendicular compression above the slab. In the WSM data of the Kermadec-Tonga subduction, some regions of the overriding plates are characterized by trench-normal compression and locally by strike-slip stress field. Compression is in agreement with our models predictions, for regions of the upper plate lying above the slab (fig. 8c-d). Such compressional tectonics is not observed in the Mariana subduction, with the exception of a small area in the southern part. Consistent with model results, stress axes rotation controlled by trench shape occurs in the Mariana subduction (fig. 8b),

where tensional axes remain always perpendicular to the trench in the upper plate. Notwithstanding the linear shape of the Kermadec-Tonga subduction, some stress axes reorientation take place in its northern part, due to a change in the trench direction (fig. 8a).

4.4.3. Lower plate

As the lower plate is concerned, our models generally show trench-perpendicular compression, related to strong coupling between upper and lower plate. Trench-perpendicular tension is clearly predicted only considering a linear subduction forced by a sustaining mantle flow (fig. 6d). On the contrary, WSM data show sparse trench perpendicular σ_3 axes in all natural cases close to the plate boundaries (fig. 7a-b and 8a-b). Compressive and strike-slip deformation appears in the lower plate of the Sumatra subduction, in regions complicated by the presence of lithospheric scale structures (e.g., the Ninety East transfer zone west of Sumatra or the Sumatra-East Java micro-plate boundary, fig. 7a).

5. Discussion

Our modeling results allow evaluating how different driving forces affect the regional stress field in subduction zones. If slab pull is the only active force (fig. 5b) the resulting stress field is controlled by the flexural bending of the sinking plate (Buffett, 2006). Down-dip tension occurs in the upper part (bending region) and compression in the deeper portion (resistance to penetration at the lower tip) of the slab. The larger the slab lateral extent, the larger the bending, owing to the greater density anomaly within the subducted lithosphere. Consistent with previous 2D results (Carminati & Petricca, 2010), if mantle flow sustains the subducted plate, intermediate down-dip tension prevails within the slab (fig. 5a), while down-dip compression prevails if the mantle flow opposes the slab (fig. 5c). This is consistent with what observed in natural subductions. Intermediate depth down-dip compression occurs in the Pacific plate in the Tonga subduction (Chen & Brudzinski, 2001; Chen et al., 2004), in the Calabrian subduction (Frepoli et al., 2007), in the Molucca and Mariana

subductions (Bailey et al., 2012), all opposed by mantle flow. Conversely, intermediate depth down-dip tension has been described in slabs sustained by the mantle flow, such as the South America (Manea et al., 2006; Bailey et al., 2012) and the Aegean subductions (Papazachos et al., 2005).

The actual improvement from using 3D models concerns the evaluation of the lateral variability of stress conditions. Substantial along-strike deformation is predicted within the subducted slabs, especially when mantle flow is applied. Along-strike tension is predicted for slabs curved in the mantle flow direction (fig. 5a and c), while along-strike compression occurs if the slab has a curvature opposing the mantle flow direction (fig. AUX3). Along-strike tension or compression resulting from flexure (forward or backward) of the slab was invoked by (Creager & Boyd, 1991) and (Chen et al., 2004) to explain lateral stress variability for the Mariana and Aleutian slabs at intermediate depths. Down-dip and along strike stress axes rotate moving towards the slab lateral edges (fig. 5a and c). It is here proposed that the local angle of incidence of the mantle flow onto the sinking slabs controls their lateral deformation, producing this rotation of stress axes.

Focusing on upper plates, many authors proposed that the stress field at crustal depths is controlled by slab geometry (e.g., Barazangi & Isacks, 1976; Ruff & Kanamori, 1980; Jordán et al., 1983; Bonnardot et al., 2008) by the efficiency of slab pull (Uyeda & Kanamori, 1979; Anderson, 2001) or by the mantle relative motion with respect to the lithosphere (e.g., Doglioni et al., 2007; Carminati & Petricca, 2010). Our models confirm these statements in the following ways. The subduction geometry exerts an important control on the stress axes orientation at shallow depths. In general, stress axes are predicted to orient perpendicular and parallel to the trench and rotate following the trench curvature (fig. 6). The stress field shows overall trench-perpendicular compression when only slab pull is applied (fig. 6a-c) or if a sustaining mantle flow is added (fig. 6d-f). An opposing mantle flow generates trench-perpendicular tension near the plate boundary (fig 6g-i). This stress pattern is consistent with the stress field described for several natural subductions (e.g., Malinverno & Ryan, 1986; Lon-

555 ergan & White, 1997; Booth-Rea et al., 2007). Trench roll-back and slab retreat
 556 were identified as the principal mechanisms originating tensional stresses in the
 557 upper plate (Doglioni, 1991; Doglioni et al., 2007; Dvorkin et al., 1993; Faccenna
 558 et al., 1996, 2001a,b; Jolivet et al., 1994), while trench-perpendicular compres-
 559 sion occurs when the overriding plate is advancing (Heuret & Lallemand, 2005;
 560 Doglioni et al., 2007). In addition, our models with opposing mantle flow display
 561 a region of the overriding plate characterized by trench-perpendicular compres-
 562 sion (fig. AUX6 d-f). This area is located within the lithosphere lying above the
 563 slab projection and is controlled by the slab pull efficiency. Is observed that the
 564 stronger the slab pull, the longer the compressional stress axes and the wider the
 565 strip of compression (fig. AUX6 d-f). This feature cannot be observed in mod-
 566 els with sustaining mantle flow, since it is summed to the overall compression
 567 which characterizes the upper plate. It is worth observing that, for opposing
 568 mantle flow and assuming lithospheric convergence rates comparable or faster
 569 than mantle flow rates (fig. AUX7), overall compression emerges in the upper
 570 plate, suggesting that convergence rate contributes to the shallow stress field.
 571 In summary, our models suggest that opposing mantle flow generates tension in
 572 the upper plate that can be partly (stripe under compression as in Fig. AUX6
 573 d f) or totally (Fig. AUX7) overcome by compression generated by slab pull
 574 and plate convergence.

575 Not all models predictions are confirmed by available data. Among natural
 576 cases of subductions sustained by mantle flow, Alaska and South America show
 577 upper-plate compression (Heuret & Lallemand, 2005) consistent with model-
 578 ing (fig. 7c-d). Sumatra, Java and Cascadia have neutral stress states. Model
 579 results and stress data match well for South America, where, in addition to com-
 580 pression in the upper plate, the stress axes rotate from north to south following
 581 the trench deflection (fig. 7b and d). Sumatra is at odds with modeling results.
 582 Here, abundant strike-slip and tension axes are observed in WSM data. No
 583 trench perpendicular compression nor clear trench-governed rotation of stress
 584 axes is recognized (fig. 7a). Oblique convergence can explain strike-slip de-
 585 formation in part of the upper plate of the Java-Sumatra subduction. Tension

could be the effect of local complex kinematics of plates involved in the Sumatra subduction (e.g., Sella et al., 2002).

A better consistency between model results and seismic data occurs for subductions forced by opposing mantle flow. Mariana, Izu-Bonin and Tonga-Kermadec are characterized by upper-plate tension (Heuret & Lallemand, 2005). As in our results, WSM tensional stress axes rotate and remain mostly perpendicular to the plate boundary in the upper plate of the Kermadec-Tonga and Mariana subductions (fig. 8). The already discussed stripe of trench-perpendicular compression predicted by models and due to the slab pull efficiency, is observed in the WSM data close to the Kermadec-Tonga trench (fig. 8a). This feature is not observed in the Mariana subduction, possibly due to more sparse data. Tonga subduction is characterized by the fastest subduction rates worldwide (Doglioni et al., 2007). Since slab pull increases with increasing subduction rate, this observation is consistent with our inference, i.e., that the stripe of compression in backarc basins is controlled by slab pull efficiency.

In the lower plates our models generally show trench-perpendicular compression. Trench-perpendicular tension is predicted for very few cases (fig. 6). Instead, WSM data show trench perpendicular tension in all natural cases close to the plate boundaries. This misfit is probably due to a larger contribution of slab bending in nature than in numerical models, possibly explained by an exceedingly stiff rheology adopted in our calculations, that do not allow for plasticity associated with large slab bending. Compressive and strike-slip deformation also appears in the lower plate of many subductions (fig. 3), such as in regions complicated by the presence of lithospheric scale structures (e.g., for Sumatra plate boundaries, fig. 7a). These observations, probably associated with local tectonic features or complex rheology, are not reproduced by our models.

It is finally emphasized that convergence rate is well constrained for tectonic plates, while the rate of net rotation of the lithosphere with respect to the mantle is largely debated (values from 2 to 13 cm/yr have been proposed; e.g., Gripp & Gordon, 2002; Steinberger et al., 2004; Cuffaro & Jurdy, 2006;

617 Crespi et al., 2007; Becker, 2008). This renders difficult a quantitative compar-
 618 ison between model results and natural observations. Oblique convergence and
 619 the occurrence of more than one plate in the subduction hanging-wall can drive
 620 other major deviations between WSM data and models. Other perturbations
 621 could be provided by anisotropy of the lithosphere, slip along complex systems
 622 of faults and processes of sediment differential compaction (Carminati et al.,
 623 2001; Carminati & Vadacca, 2010; Petricca et al., 2013).

624 6. Conclusions

625 Our 3D generic viscoelastic models emphasize the control of the system
 626 geometry on stress axes orientation in subduction zones, while mantle flow di-
 627 rection primarily controls the stress regimes within both upper and lower plates.
 628 The bending of subducting slabs generates tension in the stretching outer arc
 629 at shallow depths (< 100 km). At intermediate depths (100-300 km), down-dip
 630 tension or compression affect the slabs, depending on the flow direction of the
 631 mantle (i.e., sustaining or opposing the subducting plate). At intermediate and
 632 deeper depths, along-strike deformation is predicted by our models, especially in
 633 case of mantle flow impacting curved slabs. Along-strike tension occurs in slabs
 634 curved towards the mantle flow direction (i.e., opposing mantle over concave
 635 slabs and sustaining mantle over convex slabs), while along-strike compression
 636 occurs if the slab has an opposite curvature relative to the mantle flow direc-
 637 tion (i.e., sustaining mantle over concave slabs and opposing mantle over convex
 638 slabs). The longitudinal finiteness and curvature of the subducted lithosphere
 639 induces lateral variations and rotations of down-dip and along-strike stress axes.

640 In the shallow crust (depth of 5 km), model results show that the subduction
 641 geometry controls the stress axes orientation near the trench. Depending on the
 642 trench geometry, the stress axes rotate following the trench shape, orienting per-
 643 pendicular and parallel to the trench. In the upper plate, trench-perpendicular
 644 compression is generated in models characterized only by slab pull or when sus-
 645 taining mantle flow is forced. Trench-perpendicular tension dominates near the

646 plate boundary in case of opposing mantle flow. However, the overall extension in the upper plate is discontinued by a stripe under compression near the
647 subduction trench, especially for large slab pull. In models characterized by
648 opposing mantle flow, lithospheric convergence produces compression in both
649 the upper and the lower plate, only if convergence rate is faster than mantle
650 flow rate.
651

652 Comparing results and data from natural subductions, not all predictions
653 are confirmed. In slabs sustained by mantle flow, a good match stands out for
654 South America subduction. Here, trench-perpendicular compression in the upper
655 plate and the stress axes rotation following the trench are observed in both
656 data and results. On the contrary, Sumatra is at odds with modeling results.
657 WSM data are consistent with model results for subductions forced by opposing
658 mantle flow. Mariana and Tonga-Kermadec show upper-plate tension and
659 stress axes rotate adapting to the trench shape in the Mariana subduction. A
660 stripe of trench-perpendicular compression, possibly due to slab pull due to very
661 fast subduction rates, is present close to the Kermadec-Tonga trench, consistent
662 with model results. Our models fail to reproduce tension observed from data at
663 crustal depths in the lower plate. Misfits between model results and data may
664 be related to simplifications on assumed rheology or to local complex tectonic
665 and geological features.

666 Acknowledgments

667 This work was carried out during the PhD studies at the Department of
668 Earth Sciences, Sapienza University of Rome, and it is a part of the first author
669 PhD thesis. The constructive criticisms of two reviewers greatly improved this
670 work. Models result files, listed in the accompanying material, will be made
671 available upon request to the corresponding author. Funding from PRIN 2010-
672 2011 (Project 20107ESMX9 "Crisi e ripresa di sistemi carbonatici e potenziale
673 per la formazione di reservoir: i ruoli di clima, tettonica e magmatismo) and
674 Progetti di Ateneo 2014 is acknowledged. Discussions and support by Roberto

⁶⁷⁵ Basili, Marco Cuffaro, Carlo Doglioni and Mara M. Tiberti were very fruitful.

⁶⁷⁶ Most of the figures were produced using the GMT software.

677 **References**

- 678 Anderson, D. (2001). Top-down tectonics? *Science*, *293*, 2016–2018. doi:10.
679 1126/science.1065448.
- 680 Anderson, D. L. (1989). *Theory of the Earth*. Blackwell Scientific Publications.
- 681 Bailey, I., Alpert, L., Becker, T., & Miller, M. (2012). Co-seismic deformation
682 of deep slabs based on summed CMT data. *Journal of Geophysical Research:*
683 *Solid Earth (1978–2012)*, *117*, B04404. doi:10.1029/2011JB008943.
- 684 Barazangi, M., & Isacks, B. L. (1976). Spatial distribution of earthquakes and
685 subduction of the Nazca plate beneath South America. *Geology*, *4*, 686–692.
686 doi:10.1130/0091-7613(1976)4.
- 687 Barrientos, S. E., & Ward, S. N. (1990). The 1960 Chile earthquake: inversion
688 for slip distribution from surface deformation. *Geophysical Journal Interna-*
689 *tional*, *103*, 589–598. doi:10.1111/j.1365-246X.1990.tb05673.x.
- 690 Basili, R., Kastelic, V., Demircioglu, M., Garcia Moreno, D., Nemser, E., Pet-
691 ricca, P., Sboras, S., Besana-Ostman, G., Cabral, J., Camelbeeck, T., Caputo,
692 R., Danciu, L., Domac, H., Fonseca, J., Garcia-Mayordomo, J., Giardini, D.,
693 Glavatovic, B., Gulen, L., Ince, Y., Pavlides, S., Sesetyan, K., Tarabusi, G.,
694 Tiberti, M., Utkucu, M., Valensise, G., Vanneste, K., Vilanova, S., & Wossner,
695 J. (2013). The European Database of Seismogenic Faults (EDSF) compiled
696 in the framework of the Project SHARE, <http://diss.rm.ingv.it/SHARE-edsf>.
697 doi:10.6092/INGV.IT-SHARE-EDSF.
- 698 Becker, T. (2008). Correction to azimuthal seismic anisotropy constrains net
699 rotation of the lithosphere. *Geophysical research letters*, *35*. doi:10.1029/
700 2008GL033946.
- 701 Billen, M. I. (2008). Modeling the dynamics of subducting slabs. *Annual Review*
702 *of Earth and Planetary Sciences*, *36*, 325–356. doi:10.1146/annurev.earth.
703 36.031207.124129.

- 704 Bina, C. (1996). Phase transition buoyancy contributions to stresses in subduct-
705 ing lithosphere. *Geophysical research letters*, *23*, 3563–3566. doi:10.1029/
706 96GL03483.
- 707 Bina, C. (1997). Patterns of deep seismicity reflect buoyancy stresses due to
708 phase transitions. *Geophysical research letters*, *24*, 3301–3304. doi:10.1029/
709 97GL53189.
- 710 Bird, P., Liu, Z., & Rucker, W. K. (2008). Stresses that drive the plates
711 from below: Definitions, computational path, model optimization, and error
712 analysis. *Journal of Geophysical Research: Solid Earth (1978–2012)*, *113*.
713 doi:10.1029/2007JB005460.
- 714 Bonnardot, M.-A., Hassani, R., Tric, E., Ruellan, E., & Régnier, M. (2008).
715 Effect of margin curvature on plate deformation in a 3D numerical model
716 of subduction zones. *Geophysical Journal International*, *173*, 1084–1094.
717 doi:10.1111/j.1365-246X.2008.03752.x.
- 718 Booth-Rea, G., Ranero, C. R., Martnez-Martnez, J. M., & Grevemeyer,
719 I. (2007). Crustal types and Tertiary tectonic evolution of the Alboran
720 Sea, western Mediterranean. *Geochemistry, Geophysics, Geosystems*, *8*.
721 doi:10.1029/2007GC001639.
- 722 Brandmayr, E., Marson, I., Romanelli, F., & Panza, G. F. (2011). Lithosphere
723 density model in Italy: no hint for slab pull. *Terra Nova*, *23*, 292–299.
724 doi:10.1111/j.1365-3121.2011.01012.x.
- 725 Buffett, B. A. (2006). Plate force due to bending at subduction zones. *Jour-
726 nal of Geophysical Research: Solid Earth (1978–2012)*, *111*. doi:10.1029/
727 2006JB004295.
- 728 Carminati, E., Augier, F. T., & Barba, S. (2001). Dynamic modelling of
729 stress accumulation in Central Italy: role of structural heterogeneities and
730 rheology. *Geophysical Journal International*, *144*, 373–390. doi:10.1046/j.
731 1365-246x.2001.00323.x.

- 732 Carminati, E., Giunchi, C., Argnani, A., Sabadini, R., & Fernandez, M. (1999).
 733 Plio-Quaternary vertical motion of the Northern Apennines: insights from dy-
 734 namic modeling. *Tectonophysics*, 18, 703–718. doi:10.1029/1999TC900015.
- 735 Carminati, E., & Petricca, P. (2010). State of stress in slabs as a function
 736 of large-scale plate kinematics. *Geochemistry, Geophysics, Geosystems*, 11,
 737 Q04006. doi:10.1029/2009GC003003.
- 738 Carminati, E., & Vadacca, L. (2010). Two-and three-dimensional numerical
 739 simulations of the stress field at the thrust front of the Northern Apennines,
 740 Italy. *Journal of Geophysical Research: Solid Earth (1978–2012)*, 115. doi:10.
 741 1029/2010JB007870.
- 742 Chen, P., Bina, C., & Okal, E. (2004). A global survey of stress orientations in
 743 subducting slabs as revealed by intermediate-depth earthquakes. *Geophys-
 744 ical Journal International*, 159, 721–733. doi:10.1111/j.1365-246X.2004.
 745 02450.x.
- 746 Chen, W., & Brudzinski, M. (2001). Evidence for a large-scale remnant of
 747 subducted lithosphere beneath Fiji. *Science*, 292, 2475–2479. doi:10.1126/
 748 science.292.5526.2475.
- 749 Conrad, C., & Lithgow-Bertelloni, C. (2002). How mantle slabs drive plate
 750 tectonics. *Science*, 298, 207–209. doi:10.1126/science.1074161.
- 751 Creager, K. C., & Boyd, T. M. (1991). The geometry of Aleutian subduction:
 752 Three-dimensional kinematic flow model. *Journal of Geophysical Research:
 753 Solid Earth (1978–2012)*, 96, 2293–2307. doi:10.1029/90JB01918.
- 754 Crespi, M., Cuffaro, M., Doglioni, C., Giannone, F., & Riguzzi, F. (2007).
 755 Space geodesy validation of the global lithospheric flow. *Geophysical Journal
 756 International*, 168, 491–506. doi:10.1111/j.1365-246X.2006.03226.x.
- 757 Cuffaro, M., & Jurdy, D. M. (2006). Microplate motions in the hotspot reference
 758 frame. *Terra Nova*, 18, 276–281. doi:10.1111/j.1365-3121.2006.00690.x.

- 759 Davies, J. H., & Stevenson, D. (1992). Physical model of source region of
760 subduction zone volcanics. *Journal of Geophysical Research: Solid Earth*
761 (1978–2012), 97, 2037–2070. doi:10.1029/91JB02571.
- 762 Dickinson, W. R. (1978). Plate tectonic evolution of North Pacific rim. *Journal*
763 *of Physics of the Earth*, 26, 1–19. doi:10.4294/jpe1952.26.Supplement_S1.
- 764 Doglioni, C. (1991). A proposal for the kinematic modelling of w-dipping
765 subductions—possible applications to the Tyrrhenian–Apennines system.
766 *Terra Nova*, 3, 423–434. doi:10.1111/j.1365-3121.1991.tb00172.x.
- 767 Doglioni, C. (1993). Some remarks on the origin of foredeeps. *Tectonophysics*,
768 228, 1–20. doi:10.1016/0040-1951(93)90211-2.
- 769 Doglioni, C., Carminati, E., Cuffaro, M., & Scrocca, D. (2007). Subduction
770 kinematics and dynamic constraints. *Earth–Science Reviews*, 83, 125–175.
771 doi:10.1016/j.earscirev.2007.04.001.
- 772 Doglioni, C., Harabaglia, P., Merlini, S., Mongelli, F., Peccerillo, A., & Piro-
773 mallo, C. (1999). Orogens and slabs vs their direction of subduction. *Earth–*
774 *Science Review*, 45, 167–208. doi:10.1016/S0012-8252(98)00045-2.
- 775 Dvorkin, J., Nur, A., Mavko, G., & Ben-Avraham, Z. (1993). Narrow subducting
776 slabs and the origin of backarc basins. *Tectonophysics*, 227, 63–79. doi:10.
777 1016/0040-1951(93)90087-Z.
- 778 Dziewonski, A. M., & Anderson, D. L. (1981). Preliminary reference Earth
779 model. *Physics of the Earth and planetary interiors*, 25, 297–356. doi:10.
780 1016/0031-9201(81)90046-7.
- 781 Engdahl, E., & Scholz, C. (1977). A double Benioff zone beneath the Central
782 Aleutians: An unbending of the lithosphere. *Geophysical Research Letters*,
783 4, 473–476. doi:10.1029/GL004i010p00473.
- 784 Faccenna, C., Becker, T. W., Lucente, F. P., Jolivet, L., & Rossetti, F.
785 (2001a). History of subduction and back-arc extension in the Central Mediter-

- 786 ranean. *Geophysical Journal International*, 145, 809–820. doi:10.1046/j.
787 0956-540x.2001.01435.x.
- 788 Faccenna, C., Davy, P., Brun, J.-P., Funiciello, R., Giardini, D., Mattei, M.,
789 & Nalpas, T. (1996). The dynamics of back-arc extension: An experimental
790 approach to the opening of the Tyrrhenian Sea. *Geophysical Journal Inter-*
791 *national*, 126, 781–795. doi:10.1111/j.1365-246X.1996.tb04702.
- 792 Faccenna, C., Funiciello, F., Giardini, D., & Lucente, P. (2001b). Episodic back-
793 arc extension during restricted mantle convection in the Central Mediter-
794 ranean. *Earth and Planetary Science Letters*, 187, 105–116. doi:10.1016/
795 S0012-821X(01)00280-1.
- 796 Frank, F. (1968). Curvature of island arcs. *Nature*, 220. doi:10.1038/220363a0.
- 797 Frepoli, A., Selvaggi, G., Chiarabba, C., & Amato, A. (2007). State of stress in
798 the Southern Tyrrhenian subduction zone from fault-plane solutions. *Geo-*
799 *physical Journal International*, 125, 879–891. doi:10.1111/j.1365-246X.
800 1996.tb06031.x.
- 801 Fujii, Y., Satake, K., Sakai, S., Shinohara, M., & Kanazawa, T. (2011). Tsunami
802 source of the 2011 off the Pacific coast of Tohoku earthquake. *Earth, planets*
803 *and space*, 63, 815–820. doi:10.5047/eps.2011.06.010.
- 804 Gardi, A., Baize, S., & Scotti, O. (2010). Present-day vertical isostatic read-
805 justment of the western Alps revealed by numerical modelling and geodetic
806 and seismotectonic data. *Geological Society, London, Special Publications*,
807 332, 115–128. doi:10.1144/SP332.8.
- 808 Gardi, A., Cocco, M., Negredo, A., Sabadini, R. et al. (2002). Dynamic mod-
809 elling of the subduction zone of Central Mexico. *Geophysical Journal Inter-*
810 *national*, 143, 809–820. doi:10.1046/j.1365-246X.2000.00291.x.
- 811 Gerya, T. (2011). Future directions in subduction modeling. *Journal of Geody-*
812 *namics*, 52, 344–378. doi:10.1016/j.jog.2011.06.005.

- 813 Giunchi, C., Gasperini, P., Sabadini, R., & D'Agostino, G. (1994). The role of
814 subduction on the horizontal motions in the Tyrrhenian basin: a numerical
815 model. *Geophysical research letters*, *21*, 529–532. doi:10.1029/94GL00394.
- 816 Giunchi, C., Sabadini, R., Boschi, E., & Gasperini, P. (1996). Dynamic models of
817 subduction: geophysical and geological evidence in the Tyrrhenian Sea. *Geo-*
818 *physical Journal International*, *126*, 555–578. doi:10.1111/j.1365-246X.
819 1996.tb05310.x.
- 820 Gripp, A., & Gordon, R. (2002). Young tracks of hotspots and current plate
821 velocities. *Geophysical Journal International*, *150*, 321–361. doi:10.1046/j.
822 1365-246X.2002.01627.x.
- 823 Gudmundsson, Ó., & SambRidge, M. (1998). A regionalized upper mantle
824 (RUM) seismic model. *Journal of Geophysical Research: Solid Earth (1978–*
825 *2012)*, *103*, 7121–7136. doi:10.1029/97JB02488.
- 826 Gung, Y., Panning, M., Romanowicz, B. et al. (2003). Global anisotropy and the
827 thickness of continents. *Nature*, *422*, 707–711. doi:10.1038/nature01559.
- 828 Hasegawa, A., Umino, N., & Takagi, A. (1978). Double-planed structure of the
829 deep seismic zone in the Northeastern Japan Arc. *Tectonophysics*, *47*, 43–58.
830 doi:10.1016/0040-1951(78)90150-6.
- 831 Hashima, A., Fukahata, Y., & Matsu'ura, M. (2008). 3-d simulation of tectonic
832 evolution of the Mariana arc-back-arc system with a coupled model of plate
833 subduction and back-arc spreading. *Tectonophysics*, *458*, 127–136. doi:10.
834 1016/j.tecto.2008.05.005.
- 835 Hayes, G. P., Wald, D. J., & Johnson, R. L. (2012). Slab1.0: A three-
836 dimensional model of global subduction zone geometries. *Journal of Geophys-*
837 *ical Research: Solid Earth (1978–2012)*, *117*. doi:10.1029/2011JB008524.
- 838 Heidbach, O., Tingay, M., Barth, A., Reinecker, J., Kurfeß, D., & Müller, B.
839 (2008). The World Stress Map database. doi:10.1594/GFZ.

- 840 Heuret, A., & Lallemand, S. (2005). Plate motions, slab dynamics and back-
841 arc deformation. *Physics of the Earth and Planetary Interiors*, 149, 31–51.
842 doi:10.1016/j.pepi.2004.08.022.
- 843 Houseman, G., & Gubbins, D. (1997). Deformation of subducted oceanic litho-
844 sphere. *Geophysical Journal International*, 131, 535–551. doi:10.1111/j.
845 1365-246X.1997.tb06598.x.
- 846 Hsui, A. T., & Youngquist, S. (1985). A dynamic model of the curvature of the
847 Mariana trench. *Nature*, 318, 455–457. doi:10.1038/318455a0.
- 848 Isacks, B., & Molnar, P. (1969). Mantle earthquake mechanisms and the sinking
849 of the lithosphere. *Nature*, 223, 1121–1124.
- 850 Isacks, B., & Molnar, P. (1971). Distribution of stresses in the descending litho-
851 sphere from a global survey of focal-mechanism solutions of mantle earth-
852 quakes. *Reviews of Geophysics*, 9, 103–174. doi:10.1029/RG009i001p00103.
- 853 Jadamec, M. A., & Billen, M. I. (2010). Reconciling surface plate motions
854 with rapid three-dimensional mantle flow around a slab edge. *Nature*, 465,
855 338–341. doi:10.1038/nature09053.
- 856 Jolivet, L., Tamaki, K., & Fournier, M. (1994). Japan Sea, opening history
857 and mechanism: A synthesis. *Journal of Geophysical Research: Solid Earth*
858 (1978–2012), 99, 22237–22259. doi:10.1029/93JB03463.
- 859 Jordán, T. E., Isacks, B. L., Allmendinger, R. W., Brewer, J. A., Ramos, V. A.,
860 & Ando, C. J. (1983). Andean tectonics related to geometry of subducted
861 Nazca plate. *Geological Society of America Bulletin*, 94, 341–361. doi:10.
862 1130/0016-7606(1983)94.
- 863 Kaufmann, G., & Lambeck, K. (2000). Mantle dynamics, postglacial rebound
864 and the radial viscosity profile. *Physics of the Earth and Planetary Interiors*,
865 121, 301–324. doi:10.1016/S0031-9201(00)00174-6.

- 866 Kawakatsu, H. (1986). Double seismic zones: kinematics. *Journal of Geo-*
867 *physical Research: Solid Earth (1978–2012)*, 91, 4811–4825. doi:10.1029/
868 JB091iB05p04811.
- 869 Lallemand, S., Heuret, A., & Boutelier, D. (2005). On the relationships between
870 slab dip, back-arc stress, upper plate absolute motion, and crustal nature in
871 subduction zones. *Geochemistry, Geophysics, Geosystems*, 6. doi:10.1029/
872 2005GC000917.
- 873 Lee, C., & King, S. D. (2011). Dynamic buckling of subducting slabs reconciles
874 geological and geophysical observations. *Earth and Planetary Science Letters*,
875 312, 360–370. doi:10.1016/j.epsl.2011.10.033.
- 876 Lonergan, L., & White, N. (1997). Origin of the Betic–Rif mountain belt.
877 *Tectonics*, 16, 504–522. doi:10.1029/96TC03937.
- 878 Mahadevan, L., Bendick, R., & Liang, H. (2010). Why subduction zones are
879 curved. *Tectonics*, 29. doi:10.1029/2010TC002720.
- 880 Malinverno, A., & Ryan, W. B. (1986). Extension in the Tyrrhenian Sea and
881 shortening in the Apennines as result of Arc migration driven by sinking of
882 the lithosphere. *Tectonics*, 5, 227–245. doi:10.1029/TC005i002p00227.
- 883 Manea, V., Manea, M., Kostoglodov, V., & Sewell, G. (2006). Intraslab seismic-
884 ity and thermal stress in the subducted cocos plate beneath Central Mexico.
885 *Tectonophysics*, 420, 389–408. doi:10.1016/j.tecto.2006.03.029.
- 886 Meijer, P. T., & Wortel, M. (1999). Cenozoic dynamics of the African plate with
887 emphasis on the Africa–Eurasia collision. *Journal of Geophysical Research:*
888 *Solid Earth (1978–2012)*, 104, 7405–7418. doi:10.1029/1999JB900009.
- 889 Morra, G., Regenauer-Lieb, K., & Giardini, D. (2006). Curvature of oceanic
890 Arcs. *Geology*, 34, 877–880. doi:10.1130/G22462.1.
- 891 Nakada, M., & Lambeck, K. (1989). Late Pleistocene and Holocene Sea-level
892 change in the Australian region and mantle rheology. *Geophysical Journal*
893 *International*, 96, 497–517. doi:10.1111/j.1365-246X.1989.tb06010.x.

- 894 Negredo, A., Carminati, E., Barba, S., & Sabadini, R. (1999). Dynamic mod-
895 elling of stress accumulation in Central Italy. *Geophysical Research Letters*,
896 *26*, 1945–1948. doi:10.1029/1999GL900408.
- 897 Negredo, A., Sabadini, R., & Giunchi, C. (1997). Interplay between subduc-
898 tion and continental convergence: a three-dimensional dynamic model for
899 the central Mediterranean. *Geophysical Journal International*, *131*, f9–f13.
900 doi:10.1111/j.1365-246X.1997.tb00590.x.
- 901 Norton, I. O. (2000). Global hotspot reference frames and plate motion. *Geo-*
902 *physical Monograph Series*, *121*, 339–357. doi:10.1029/GM121p0339.
- 903 Obayashi, M., Yoshimitsu, J., Nolet, G., Fukao, Y., Shiobara, H., Sugioka, H.,
904 Miyamachi, H., & Gao, Y. (2013). Finite frequency whole mantle P wave
905 tomography: Improvement of subducted slab images. *Geophysical Research*
906 *Letters*, *40*, 5652–5657. doi:10.1002/2013GL057401.
- 907 Panza, G., Doglioni, C., & Levshin, A. (2010). Asymmetric ocean basins. *Ge-*
908 *ology*, *38*, 59–62. doi:10.1130/G30570.1.
- 909 Papazachos, B., Dimitriadis, S., Panagiotopoulos, D., Papazachos, C., & Pa-
910 padimitriou, E. (2005). Deep structure and active tectonics of the Southern
911 Aegean volcanic Arc. In M. Fytikas (Ed.), *The South Aegean Active Volcanic*
912 *Arc* (pp. 47–64). Developments in Volcanology volume 7.
- 913 Petricca, P., Carafa, M., Barba, S., & Carminati, E. (2013). Local, regional,
914 and plate scale sources for the stress field in the Adriatic and PeriAdri-
915 atic region. *Marine and Petroleum Geology*, *42*, 160–181. doi:10.1016/j.
916 marpetgeo.2012.08.005.
- 917 Quinteros, J., & Sobolev, S. V. (2013). Why has the Nazca plate slowed since
918 the Neogene? *Geology*, *41*, 31–34. doi:10.1130/G33497.1.
- 919 Ricard, Y., Doglioni, C., & Sabadini, R. (1991). Differential rotation between
920 lithosphere and mantle: A consequence of lateral mantle viscosity variations.

- 921 *Journal of Geophysical Research: Solid Earth* (1978–2012), *96*, 8407–8415.
922 doi:10.1029/91JB00204.
- 923 Rodríguez-González, J., Negredo, A. M., & Carminati, E. (2014). Slab–mantle
924 flow interaction: influence on subduction dynamics and duration. *Terra Nova*,
925 *26*, 265–272. doi:10.1111/ter.12095.
- 926 Ruff, L., & Kanamori, H. (1980). Seismicity and the subduction process.
927 *Physics of the Earth and Planetary Interiors*, *23*, 240–252. doi:10.1016/
928 0031-9201(80)90117-X.
- 929 Schellart, W., Freeman, J., Stegman, D., Moresi, L., & May, D. (2007). Evolu-
930 tion and diversity of subduction zones controlled by slab width. *Nature*, *446*,
931 308–311. doi:10.1038/nature05615.
- 932 Sella, G. F., Dixon, T. H., & Mao, A. (2002). Revel: A model for recent plate
933 velocities from space geodesy. *Journal of Geophysical Research: Solid Earth*
934 (1978–2012), *107*, ETG–11. doi:10.1029/2000JB000033.
- 935 Seno, T., & Yamanaka, Y. (1996). Double seismic zones, compressional deep
936 trench–outer rise events, and superplumes. *Geophysical Monograph Series*,
937 *96*, 347–355. doi:10.1029/GM096p0347.
- 938 Spada, G., Ricard, Y., & Sabadini, R. (1992). Excitation of true polar wander
939 by subduction. *Nature*, *360*, 452–454. doi:10.1038/360452a0.
- 940 Stein, S., & Okal, E. A. (2005). Seismology: Speed and size of the sumatra
941 earthquake. *Nature*, *434*, 581–582. doi:10.1038/434581a.
- 942 Steinberger, B., Sutherland, R., & O’connell, R. (2004). Prediction of Emperor–
943 Hawaii Seamount locations from a revised model of global plate motion and
944 mantle flow. *Nature*, *430*, 167–173. doi:10.1038/nature02660.
- 945 Tetzlaff, M., & Schmeling, H. (2009). Time–dependent interaction between
946 subduction dynamics and phase transition kinetics. *Geophysical Journal In-*
947 *ternational*, *178*, 826–844. doi:10.1111/j.1365-246X.2009.04182.x.

- 948 Uyeda, S. (1981). Subduction zones and back Arc basins – A review. *Geologische*
949 *Rundschau*, 70, 552–569. doi:10.1007/BF01822135.
- 950 Uyeda, S., & Kanamori, H. (1979). Back-arc opening and the mode of subduc-
951 tion. *Journal of Geophysical Research: Solid Earth (1978–2012)*, 84, 1049–
952 1061. doi:10.1029/JB084iB03p01049.
- 953 Williams, C. A., & Richardson, R. M. (1991). A rheologically layered three-
954 dimensional model of the San Andreas fault in Central and Southern Califor-
955 nia. *Journal of Geophysical Research: Solid Earth (1978–2012)*, 96, 16597–
956 16623. doi:10.1029/91JB01484.
- 957 Yoshii, T. (1973). Upper mantle structure beneath the north Pacific and the
958 marginal seas. *Journal of Physics of the Earth*, 21, 313–328. doi:10.4294/
959 jpe1952.21.313.
- 960 Zhao, D. (2004). Global tomographic images of mantle plumes and subducting
961 slabs: insight into deep Earth dynamics. *Physics of the Earth and Planetary*
962 *Interiors*, 146, 3–34. doi:10.1016/j.pepi.2003.07.032.
- 963 Zhong, S., Gurnis, M., & Moresi, L. (1998). Role of faults, nonlinear rheology,
964 and viscosity structure in generating plates from instantaneous mantle flow
965 models. *Journal of Geophysical Research: Solid Earth (1978–2012)*, 103,
966 15255–15268. doi:10.1029/98JB00605.

Table 1: Main constants and expressions used for the Earth's layers in viscoelastic models. The subscripts indicate the described layer: crust (*cr*), lithosphere (*lit*), upper mantle (*um*) and lower mantle (*lm*).

Parameter	Value	Units	Description
E_{cr}	60×10^9	Pa	Elastic modulus
η_{cr}	1×10^{24}	$Pa \cdot s$	Viscosity
G_{cr}	3.75×10^4	MPa	Shear modulus
E_{lit}	1.75×10^{11}	Pa	Elastic modulus
η_{lit}	5×10^{22}	$Pa \cdot s$	Viscosity
G_{lit}	1.11×10^5	MPa	Shear modulus
E_{um}	1.75×10^{11}	Pa	Elastic modulus
η_{um}	1×10^{21}	$Pa \cdot s$	Viscosity
G_{um}	1.11×10^5	MPa	Shear modulus
E_{lm}	1.27×10^{11}	Pa	Elastic modulus
η_{lm}	1×10^{22}	$Pa \cdot s$	Viscosity
G_{lm}	8×10^4	MPa	Shear modulus

Table 2: List of developed 3D models and geometries dimension. All the modeled geometries were tested applying different mantle flow (0-8 cm/yr) and plate convergence (0-5 cm/yr) velocities. Summaries of models and applied kinematics are provided in the auxiliary material.

Model name	Reference figure	Model lenght/width/depth (km)	slab (halved) lateral extent (km)
3D Linear trench			
L3D-500	figure 4b	2000x1250x1000	500
L3D-1000		2000x1500x1000	1000
L3D-3000		2000x2500x1000	1500
3D Curved trench - concave slab			
CCV3D-20	figure 4c	2350x2000x1000	500
CCV3D-50		2350x2000x1000	1000
CCV3D-80		2350x2000x1000	1500
3D Curved trench - Convex slab			
CVX3D-20	figure 4d	2350x2000x1000	500
CVX3D-50		2350x2000x1000	1000
CVX3D-80		2350x2000x1000	1500

Table 3: Compilation of the main subduction zones of fig. 3 with indications about the trench geometry (i.e., linear, curved or variable along-strike), the mantle flow direction relative to the slab dip (SMF=sustaining mantle flow; EMF=opposing mantle flow), the plate convergence (HS3 reference frame; Gripp & Gordon, 2002) and the kind of deformation affecting the upper plate (UPS: C=compressional; N=neutral; T=tensional).

Subduction name	Reference figure	Trench shape	SMF	EMF	P. convergence (mm/yr)	UPS
S. America	3a	mixed	X		14 – 78	C-N
Sumatra	3b	curved	X		32 – 77	N
C. America	3c	linear	X		29 – 50	N
Vanuatu	3d	mixed	X		54 – 84	N
Solomon	3e	mixed	X		32 – 50	C-N
Aleutians	3f	curved		X	46 – 84	N
Kermadec	3g	linear		X	145 – 220	T-N
Ryukyu	3h	linear		X	24 – 63	T-N
Izu-Bonin	3i	mixed		X	21 – 102	T
Philippines	3j	linear		X	97 – 106	N-C

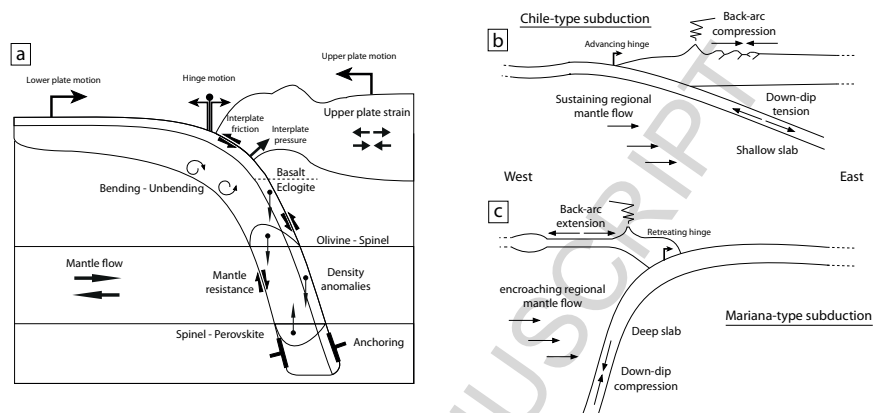


Figure 1: **Subduction dynamics.** a) Principal driving and resisting forces for subducting lithosphere (modified after Billen (2008) and Lallemand et al. (2005)). Phase changes affecting the density of rocks are also indicated. Plate kinematics, mantle motions and upper plate strain are indicated by arrows; b) Chilean and c) Mariana end-member types of subduction zones (modified after Uyeda & Kanamori, 1979), differ because of the geometry, the subduction direction relative to the mantle flow and the stress field affecting the upper and the lower plates.

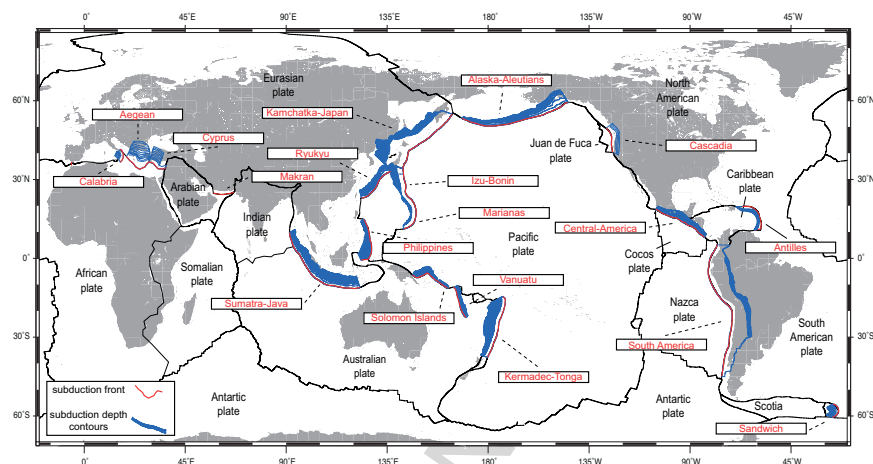


Figure 2: **Active subduction zones and major plate boundaries (black lines).** Red lines indicate the trench and blue lines the contours of slab every 100 km. Calabria, Aegean and Cyprus slab contours are from the SHARE-edsf database (Basili et al., 2013). Antilles and South-Philippines slab contours are from the RUM-database (Gudmundsson & SambRidge, 1998). The remaining subduction contours are from the slab 1.0 database (Hayes et al., 2012). The name of the subduction systems are reported in the text boxes.

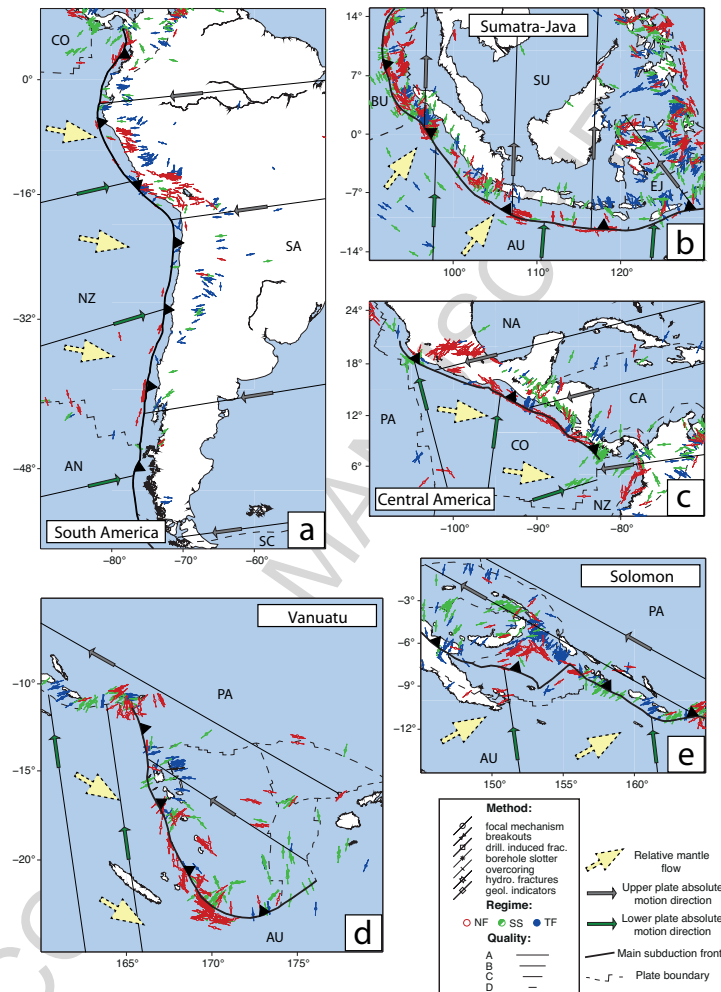


Figure 3: stress field (0-50 km depth) for the principal subduction zones. Direction of the largest horizontal principal axes (SHmax) for thrust (blue), normal (red) and strike-slip (green) stress regimes is shown (data after Heidbach et al., 2008). Plate boundaries ((after Bird et al., 2008) and coastlines are shown as black lines. NZ (Nazca), CO (Cocos), SA (S. America), AN(Antarctica), SC(Scotia), SU(Sunda), BU(Burma), EJ(E-Java), AU (Australia), NA (N-America), CA (Caribbean), PA (Pacific), KE (Kermadec), AM (Amur), MA (Mariana), PS (Philippine), YA (Yangtze). Green and gray arrows indicate the absolute motion directions for the lower and the upper plates (after Gripp & Gordon, 2002). Yellow dashed arrows represent the relative motion of the global mantle flow (modified from Doglioni et al., 1999). Black arrows indicate the mean dip direction of the slabs. Note that in panels a-e the mantle motion sustain the slab. In panels f-j the mantle motion opposes slab dip

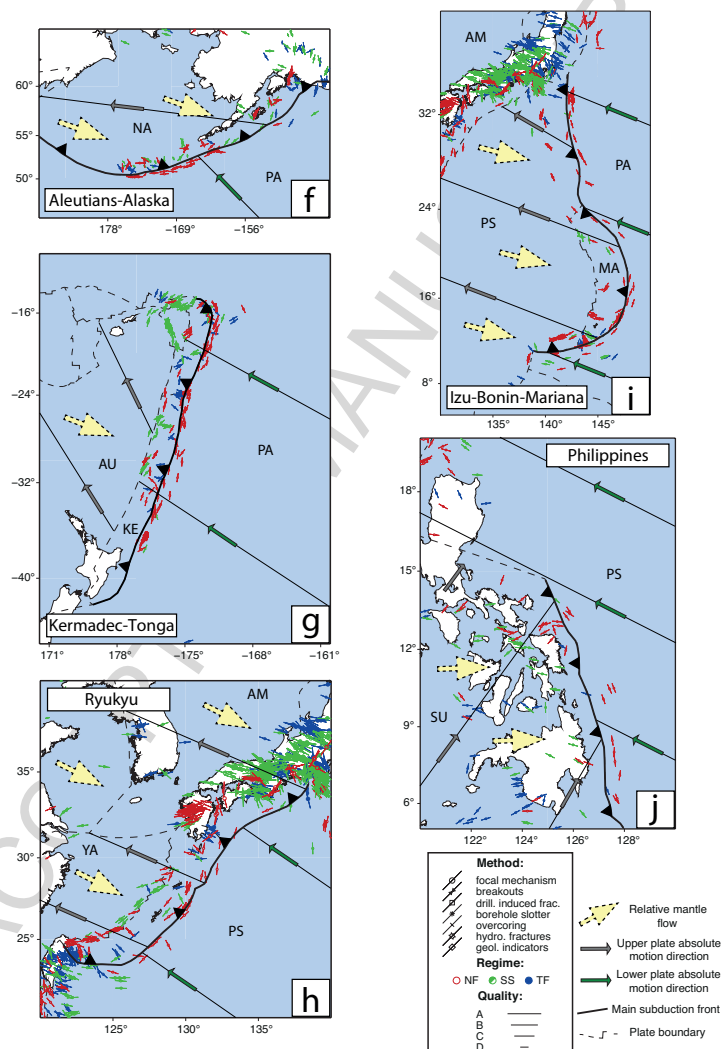


Figure 3 (continued)

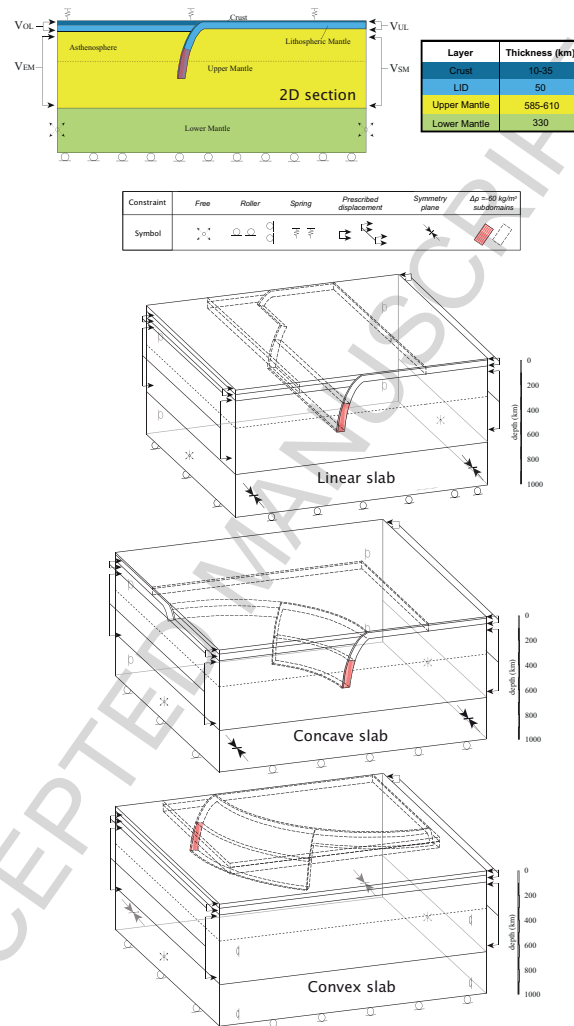


Figure 4: **Geometry, materials, and boundary conditions of the models reproducing the three classes described in the text.** a) In 2D a dotted line shows the base of the asthenosphere. When modeled, a density contrast was applied to the areas marked by the red grid (in 2D) or down to the dashed plane within the subducted lithosphere (in 3D). V_{OL} (velocity of the overriding plate), V_{UL} (velocity of the underlying plate), V_{EM} (velocity of the mantle at the left boundary, i.e. opposing the slab), and V_{SM} (velocity of the mantle at the right boundary, i.e. sustaining the slab) are applied as boundary conditions. The symbols are explained in the central panel. Bright symbols refer to hidden planes. Only the intermediate-length geometry is shown for both linear and curved 3D models (see text for explanations). The front boundary surfaces of the linear b) and the curved concave c) slab models are symmetry planes. Instead, the back plane is symmetric for the curved 3D model with convex slab d).

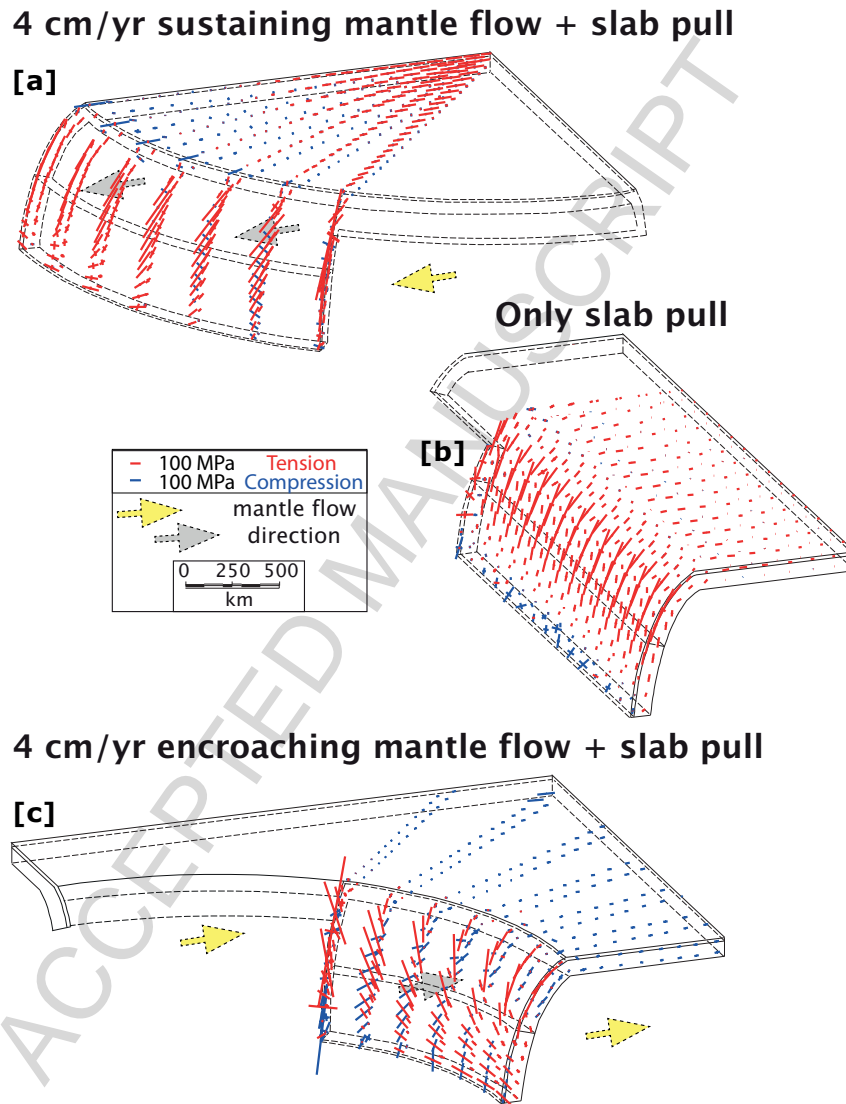


Figure 5: **Prospective view of the 3D linear and curved shaped geometries results.** Results are shown for models simulating: a) slab pull plus a sustaining mantle flow forcing a convex subducting slab, b) linear slab forced only by slab pull, c) slab pull plus an opposing mantle flow forcing a concave subducting slab. Yellow arrows indicate the mantle flow direction and velocity. Stress axes are plotted at crustal (5 km) and at lithospheric (50 km) depths within the lower plate, and follow the adopted depths within the sinking slabs. Upper plates are not shown.

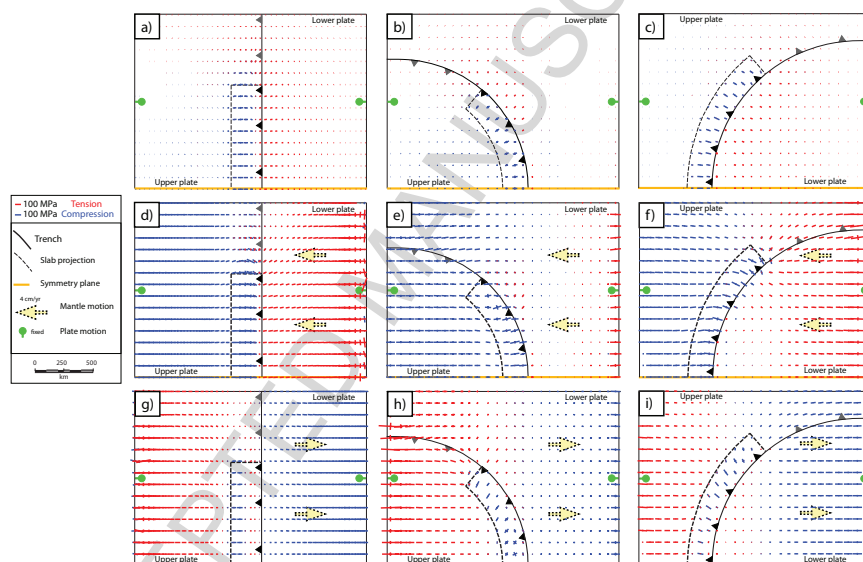


Figure 6: Map view showing the stress field predicted at crustal depth (5 km) by 3D models with linear and curved trench geometries. Results are referred to models: forced by only slab pull (panels a-c); characterized by slab pull and 4 cm/yr mantle flow sustaining the slab (panels d-f); forced by slab pull and 4 cm/yr mantle flow opposing the slab (panels g-i). No plate convergence is included.

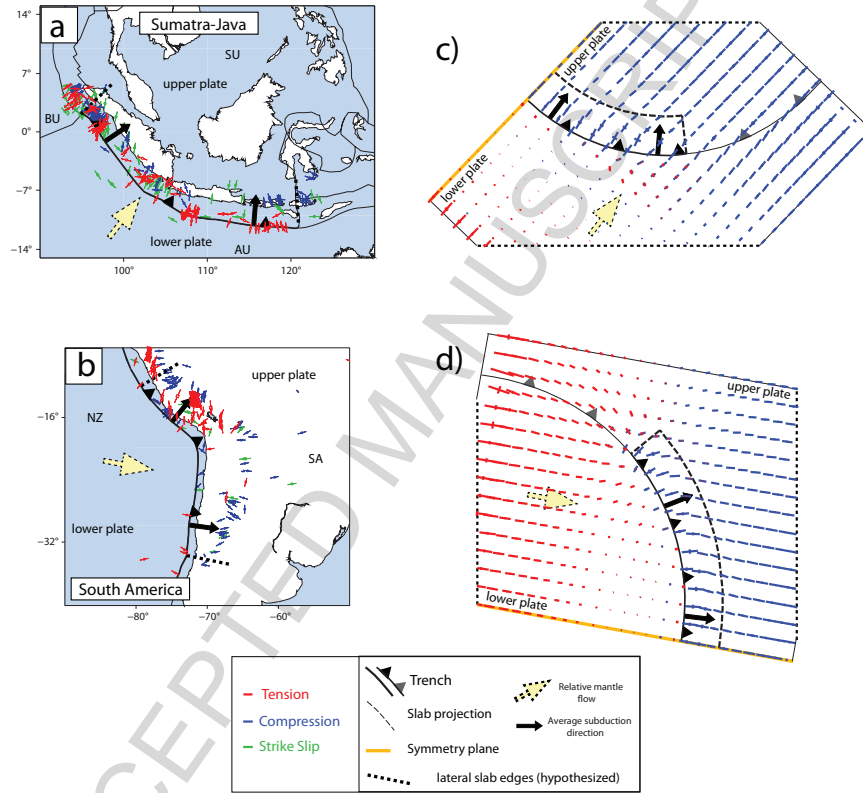


Figure 7: Intraplate stress orientation (0-50 km depth) for the sustaining mantle flow subduction zone cases. Direction of the stress axes for (blue) compressional (σ_1), (red) tensional (σ_3) and (green) strike-slip (σ_1) stress regimes is shown for the a) Sumatra and b) South America (data after Heidbach et al., 2008). Major plates are named as in fig. 3. Lateral edges of natural slabs are indicatively represented with black dashed-thick lines. Map view of the principal stress axes at crustal depth (5 km) within both the lower and the upper plates obtained with 3D models with linear and curved trench geometries forcing slab pull and 4 cm/yr mantle flow sustaining the slab. No convergence is imposed.

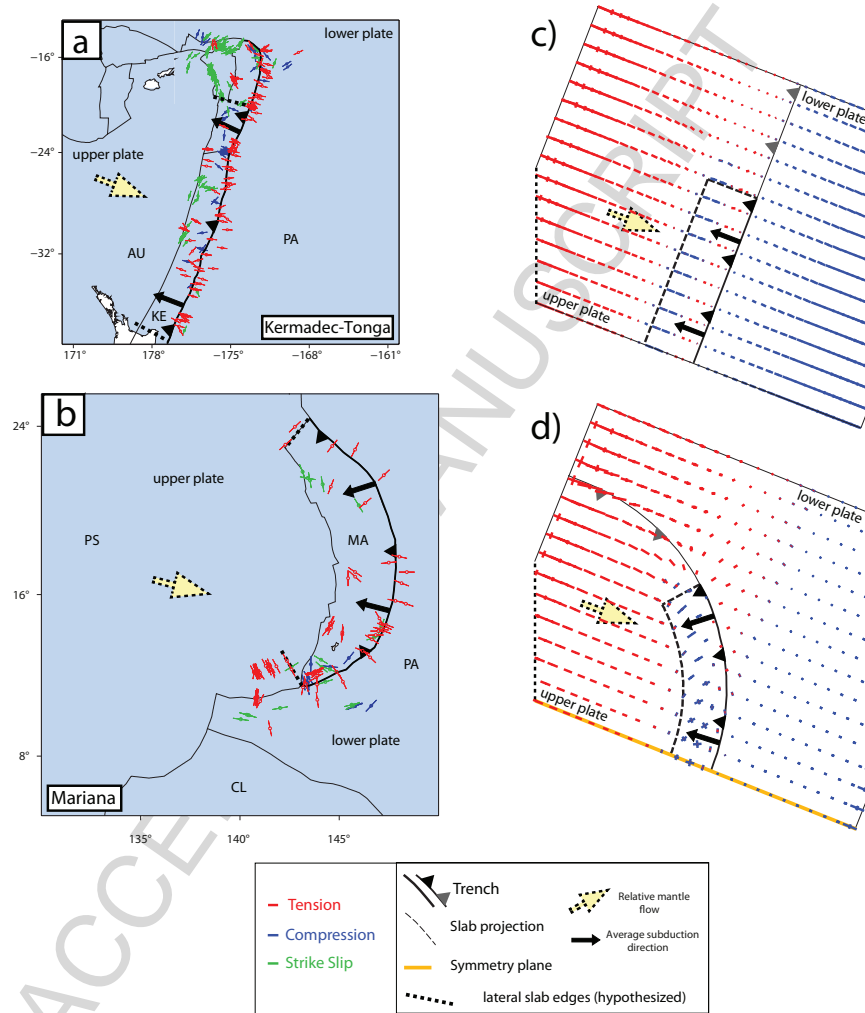


Figure 8: **Intraplate stress orientation (0-50 km depth) for the opposite mantle flow subduction zone cases.** Direction of the stress axes for (blue) compressional (σ_1), (red) tensional (σ_3) and (green) strike-slip (σ_1) stress regimes is shown for the a) Kermadec and b) Mariana subduction zones (data after Heidbach et al., 2008). Major plates are named as in fig. 3. Map view of the principal stress axes at crustal depth (5 km) within both the lower and the upper plates obtained by 3D models with linear and curved trench geometries forcing slab pull and 4 cm/yr mantle flow opposing the slab. No convergence is imposed.

Comparison of 3D viscoelastic FEMs and present-day stress field data
Role of kinematics and subduction geometry in generating the observables
Mantle flow direction controls the stress regimes within plates
The trench curvature induces stress axes rotations at crustal depths
Along-strike deformation is predicted at intermediate and deeper depths
in slabs